

Facial Depth and Normal Estimation using Single Dual-Pixel Camera

Minjun Kang^{1†} Jaesung Choe¹ Hyowon Ha⁴ Hae-Gon Jeon² Sunghoon Im³ In So Kweon¹

KAIST¹

GIST²

DGIST³

FACEBOOK⁴

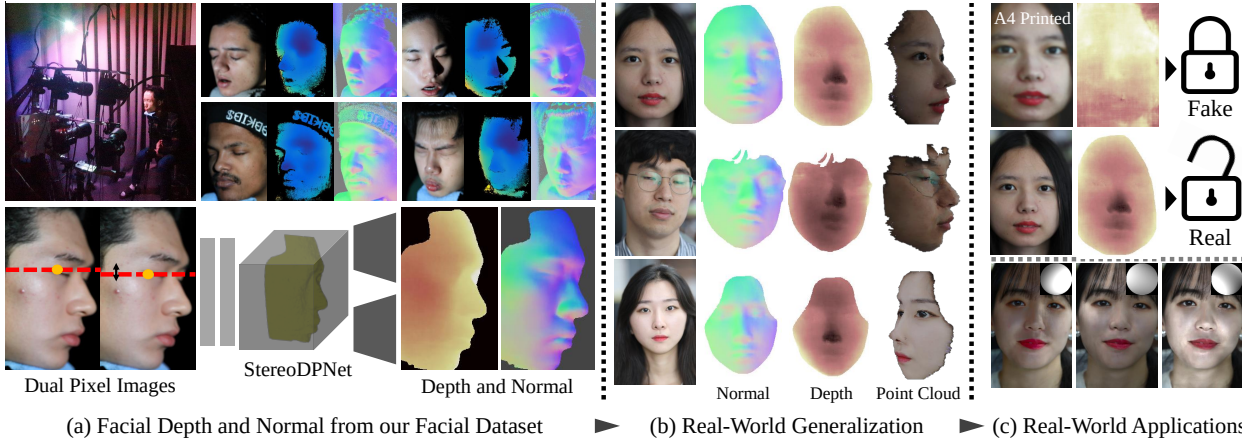


Figure 1. Using our Dual-Pixel facial dataset (a), our method aims at generalized estimation of unmet facial geometry (b), which can be used for various applications, such as face anti-spoofing or facial relighting (c).

Abstract

Many mobile manufacturers recently have adopted Dual-Pixel (DP) sensors in their flagship models for faster auto-focus and aesthetic image captures. Despite their advantages, research on their usage for 3D facial understanding has been limited due to the lack of datasets and algorithmic designs that exploit parallax in DP images. This is because the baseline of sub-aperture images is extremely narrow and parallax exists in the defocus blur region. In this paper, we introduce a DP-oriented Depth/Normal network that reconstructs the 3D facial geometry. For this purpose, we collect a DP facial data with more than 135K images for 101 persons captured with our multi-camera structured light systems. It contains the corresponding ground-truth 3D models including depth map and surface normal in metric scale. Our dataset allows the proposed matching network to be generalized for 3D facial depth/normal estimation. The proposed network consists of two novel modules: Adaptive Sampling Module and Adaptive Normal Module, which are specialized in handling the defocus blur in DP images. Finally, the proposed method achieves state-of-the-art performances over recent DP-based depth/normal estimation methods. We also demonstrate the applicability of the estimated depth/normal to face spoofing and relighting.

1. Introduction

A huge number of facial images are posted every day on social media. In 2020, for example, about 70 percent of photos were taken using cameras on smartphones and 24 billion selfies were uploaded to Google Photos App [16, 17]. Many users create their own photos with a uniquely personal, aesthetic, and creative touch, prior to uploading them. Of course, such effects are more natural when the facial geometry is given [5, 54, 61]. Face anti-spoofing also requires 3D facial geometry to accurately identify an authorized person's face and prevent false facial verification [59]. Recently, acquiring facial geometry in smartphones and DSLR cameras has emerged as an interesting research topic. One can accomplish this by either using multiple cameras [4, 14] or active sensing devices [25, 27]. However, these methods suffer from uncontrolled lighting conditions and their performances heavily relies on the hardware synchronization and the color calibration.

More recently, many mobile manufacturers have used Dual-Pixel (DP) sensors in their flagship models to support faster auto-focus and more aesthetic image captures. DP images are perfectly synchronized with the same exposure, white balance and geometric rectification. The im-

[†] Email address : kmmj2005@kaist.ac.kr

ages can be regarded as stereo images [15] with a narrow baseline. Exploiting the advantages of DP images, previous studies [15, 35, 36, 48, 60] have demonstrated that DP images can be utilized to estimate scene depths within the certain ranges of scenes. Despite strengths of DP images, there has been limited study [52] to recover a facial geometry from a Dual-Pixel camera. This is due to the lack of facial DP dataset with precise 3D geometry and an appropriate architectural design. Moreover, it is challenging to infer depths from homogeneous human faces using DP sensors.

To address the issues, we present a large-scale DP-oriented 3D facial dataset and Depth/Normal network (stereoDPNet). This work aims to recover 3D facial geometry from a DP sensor through our carefully designed network trained on the dataset. Our facial geometry dataset involves 135,744 face data for 101 persons consisting of DP images, depth maps, and surface normal maps. Finally, the contributions are summarized as follows:

- A large-scale DP-oriented 3D facial dataset with more than 135K DP images and their corresponding high-quality 3D models taken from a structured light system.
- A novel depth/normal network for generalized estimations of facial 3D reconstruction using DP images.
- Practical usage in the real-world (unseen and uncontrolled environments) including face anti-spoofing and facial relighting.

2. Related Work

Defocus-disparity in Dual-Pixel. Dual-Pixel images can be considered as a pair of stereo images since the DP camera captures two sub-aperture images with small parallax. However, since the DP camera is equipped with a micro-lens array in front of a camera sensor, the pixel disparity in DP images is extremely narrow ($-4\text{px} \sim +4\text{px}$) [60] compared to conventional stereo images. For this reason, Zhang *et al.* [60] contend that monocular DP images are not suitable for cost volume-based disparity regression due to the narrow baseline ($< \sim 1\text{mm}$). Other works [15] also adopt simple 2D U-Net architectures for affine-transformed depth regression. Meanwhile, the disparity of DP images is induced by different left/right point spread functions (PSFs) instead of view parallax of stereo, called defocus-disparity [36]. Based on this observation, Punnappurath *et al.* [36] propose an optimization-based disparity regression using a parametrized PSF. The pioneering works [15, 36, 48] allow us to formulate a depth to disparity conversion model. **Geometry dataset for Dual-Pixel.** Owing to the growing research interest in DP photography, several real/synthetic DP datasets [3, 15, 35, 36] have been released. Garg *et al.* [15] propose a real-world DP dataset that includes scene-scale images captured by an array of smartphones. Despite

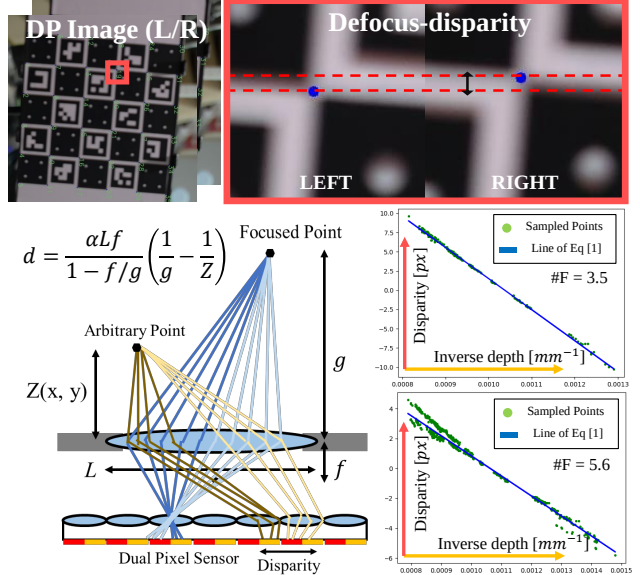


Figure 2. **Dual-Pixel Geometry.** Disparity in DP images exists in blurry regions, called defocus-disparity (upper). The ground-truth depth obtained by a plane homography and a defocus-disparity from the matching pairs are used to robustly find parameters of Eq. 1 (bottom left). This relationship is used to back-project our prediction to metric-scale depth (bottom right).

of their success, the estimated depth is up to scale because their training data is a relative-scaled 3D geometry computed by a multiview stereo algorithm (COLMAP [41]).

Face dataset. Facial datasets have typically been created whenever new types of commercial imaging devices are introduced. Since it is only available to reconstruct faces from monocular images with a limited assumption [51], many 3D face regression methods [13, 18, 39] rely on a given face morphable model [7, 47] and modify the shape with facial keypoints [13, 43] and landmarks [6, 12]. Recently, several face regression models [6, 50] utilize multi-view images as input. However, it is challenging to estimate facial geometry from DP image since blurry regions are hardly captured from homogeneous faces. This property brings difficulty in finding correspondence between left/right DP images. We observe that the previous DP-oriented methods [15, 36] have difficulty estimating the 3D geometry of human faces as well. Many of the applications with facial images require both a high-quality depth and a surface normal for pleasing aesthetic effects [61]. Therefore, we satisfy the increasing industrial and academic demands by providing high-quality and absolute scale facial depth/normal maps that are captured with cameras with DP sensors.

3. Facial Dataset with Dual-Pixel

In this section, we explain the construction of DP-oriented facial dataset. We first describe a ground-truth depth/normal acquisition process (Sec. 3.1), then explain the data configuration (Sec. 3.2), and details of capturing

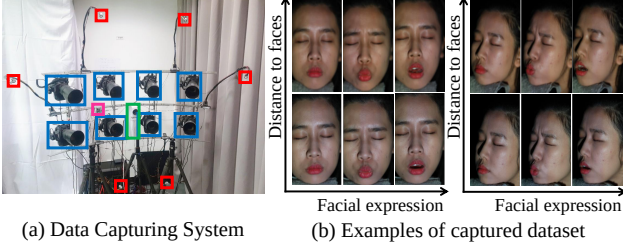


Figure 3. **Examples of our facial dataset.** (a) The proposed hardware setup: (2×4 multi-camera array (blue), 6 LEDs (red), a projector (green), and a LED controller (magenta)). (b) DP images with various facial expressions (horizontal axis) and distances from the hardware to faces (vertical axis). There are two additional images taken in different heading directions (center/rightward).

system (Sec. 3.3).

3.1. Ground Truth Data Acquisition

Structured light systems are designed for high-quality 3D geometry acquisition under controlled environments by projecting pre-defined patterns on surfaces of objects [11, 20, 40] and by analyzing the projected patterns to measure 3D shapes of the objects. It is extensively used for ground-truth depth maps in stereo matching benchmarks [1, 23, 46] and shape from shading [21]. In this work, we tailor the structured light-based facial 3D reconstruction method [19] with our well-synchronized multi-camera system. Moreover, we calibrate point light directions by using a chrome ball and apply a photometric stereo in [34] to obtain accurate surface normal maps of subjects’ faces in Fig. 4(d). By using the surface normals, initial depth is refined by conforming the initial facial depth and the surface normal [34], whose examples are illustrated in Fig. 4(a), (b) and (c).

To the end, we find an exact conversion between a defocus-disparity and a metric depth by using the relationship of signed defocus-blur $\bar{b}(x, y)$ and disparity d (Eq. 1) introduced in [15].

$$\begin{aligned} d(x, y) &= \alpha \bar{b}(x, y) \\ &\approx \alpha \frac{Lf}{1 - f/g} \left(\frac{1}{g} - \frac{1}{Z(x, y)} \right) \\ &\triangleq A(L, f, g) + \frac{B(L, f, g)}{Z(x, y)}, \end{aligned} \quad (1)$$

where $(x, y, Z(x, y))$ indicates 3D coordinates in camera space, α is a proportional term, and L is the diameter of the camera aperture. f represents the focal length of the lens and g is the focus distance of the camera. By using this relationship, we obtain a ground-truth defocus-disparity from the ground-truth depth in Fig. 2. This conversion is used to back-project our defocus-disparity to metric 3D space, and will be utilized to encode absolute metric information for our depth and surface normal estimation network in Sec. 4.

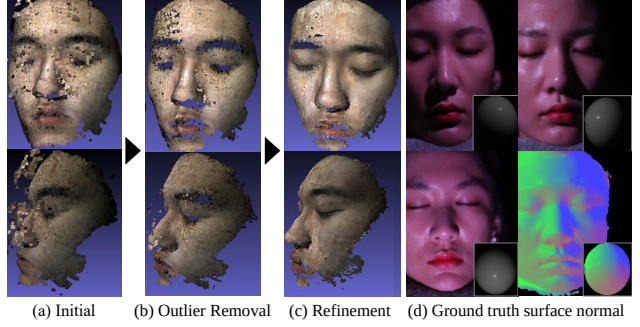


Figure 4. **Ground-truth depth and surface normal acquisition.** (a) Initial depth from the structured light. (b) Depth after removing outliers. (c) Ground-truth depth via fusion of the initial depth and the surface normal obtained from the photometric stereo in (c).

3.2. Dataset Configuration

Given an array of multiple DP cameras, we capture various human faces with different expressions and light conditions. The dataset consists of 135,744 photos, which are a combination of 101 people, eight cameras, seven different lighting condition, four facial heading directions (left, right, center and upward), three facial expressions (normal, open mouth and frown), and two fixed distances of subjects from the camera array, as illustrated in Fig. 3. The distances between the camera array and subjects range from 80 cm to 110 cm. Our dataset includes 44,352 female photos as well as 91,392 male photos, and their ages range from 19 to 45, and detailed statistics are provided in the supplementary material. In main experiments, we use 76 people (76%) as the training dataset and the others (24%) as a test/validation dataset without any overlap with the training set.

3.3. Hardware Setup

For facial data acquisition, we set up the DP-oriented camera-projector system. The system consists of eight synchronized Canon 5D Mark IV cameras on a 2×4 grid, with one commercial projector (1920×1080 pixels) and six LED lights, as shown in Fig. 3. These cameras are available to capture DP images [2, 3, 35]. Each camera is equipped with a Canon 135mm L lens. The 17° field of view (FOV), which the lens affords, can cover an approximately $16.7\text{cm} \times 25\text{cm}$ area at about one-meter distance, which is suitable for capturing human faces. We take our dataset with a camera aperture of F5.6, exposure time $1/30''$, and ISO 1600. The shape of the camera rig mimics a spherical dome with a one-meter radius. All of the cameras are located on the rig looking at the same point near the sphere’s center, where a target object is placed. The projector is positioned at the center of the camera array. The LED lights are installed at various positions so that face images can be taken under varying lighting conditions.

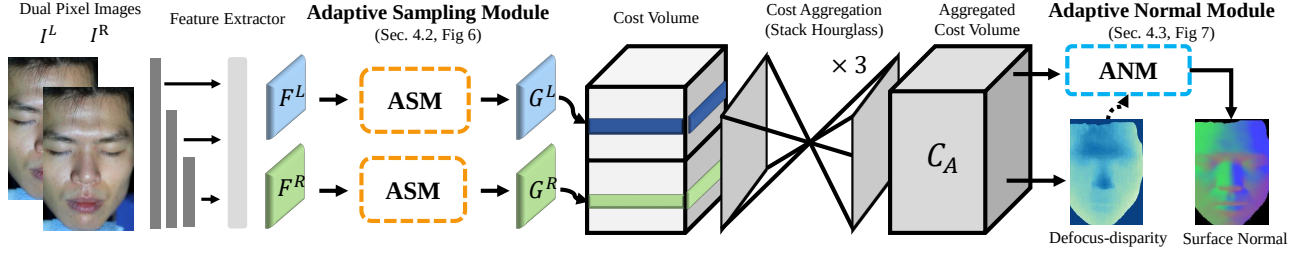


Figure 5. **Architecture of StereoDPNet.** Given DP images, our network is trained to infer facial depth/normal maps. Our two key modules, Adaptive Sampling Module and Adaptive Normal Module, overcome the extremely narrow baseline in DP images by capturing disparities in blurry regions. Note that we use the pre-defined relationship between disparity and depth in Sec. 3.1 to convert disparity to metric depth.

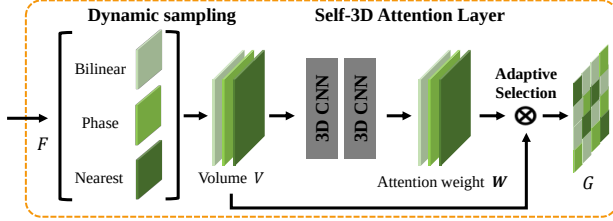


Figure 6. **Architecture of ASM.** Adaptive Sampling Module consists of a dynamic sampling and a self-3D attention layer.

4. Facial Depth and Normal Estimation

We design a Dual-Pixel oriented Depth/Normal network (StereoDPNet) that estimates both defocus-disparity and surface normal in an end-to-end manner as shown in Fig. 5. The network is trained on our dataset of facial DP images paired with high quality 3D geometry.

4.1. Overall Architecture

As shown in Fig. 5, StereoDPNet consists of four parts: feature extraction layer, Adaptive Sampling Module (ASM), cost aggregation layer, and Adaptive Normal Module (ANM). Given DP images with left I^L and right I^R viewpoints, the feature extraction layer infers DP image features F^L and F^R , respectively. Our feature extractor captures multi-scale information with a large receptive field by adopting Atrous Spatial Pyramid Pooling [10] and Feature Pyramid Network [31] to encode various sizes of defocus blur in the DP images. Given the extracted features F^L and F^R , the proposed ASM in Fig. 6 captures an amount of spatially varying blur in dynamic ranges, and then adaptively samples the features. The sampled features G^L and G^R are stacked into a cost volume, and the volume is aggregated through three stacked hourglass modules. The aggregated cost volume C_A is used to regress both defocus-disparity and surface normal by ANM in Fig. 7. The details of ASM and ANM are described in Sec. 4.2 and Sec. 4.3.

4.2. Adaptive Sampling Module

Since the defocus-disparity is computed by the various sizes of blur within a small range of values, its baseline has a narrow ranges compared to the conventional stereo

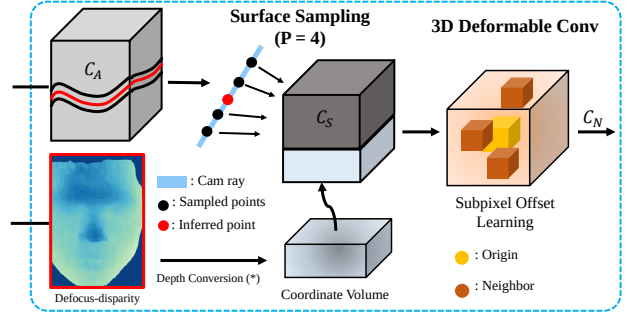


Figure 7. **Architecture of ANM.** Adaptive Normal Module consists of a surface sampling and a 3D deformable convolutional layer for surface normal regression.

matching [8, 26, 53, 56]. The typical stereo matching methods focus on finding correspondences between two all-in-focus images. On the contrary, the DP-based stereo matching must handle the narrow baseline issue as well as defocus blur in DP images. To address these issues, we design the Adaptive Sampling Module (ASM).

The network design of ASM is inspired by the best practices of defocus blur matching [9] and depth from narrow-baseline light-field image [24]. We design a network that captures blurry texture features to estimate the relative blur, and a dynamic sampling strategy for narrow-baseline stereo matching, as illustrated in Fig. 6. ASM learns to take an amount of blur from a textured region in DP images I^L, I^R and to generate disparity hypotheses with sub-pixel accuracy. As a result, ASM plays a role in computing matching costs for blurry regions with the image features F^L, F^R . To this end, the features pass through a *dynamic feature sampling layer* and a *self-3D attention layer* to obtain the sampled features G^L, G^R .

The dynamic sampling layer is designed with a combination of nearest-neighbor, bilinear, and phase-shift interpolation. Because the DP images have a narrow baseline, a sub-pixel level shift operation is required. However, the sub-pixel shift from different sampling strategies provides varying results depending on the local scene configurations in [24]. To take advantage of conventional sampling methods, we incorporate them into ASM. In particular, phase-shift interpolation ensures a denser sampling field at sub-

pixel precision and reduces the burden from blurriness compared to other interpolation methods [24]. In the end, the shifted features from the three different sampling strategies are concatenated into one channel as a volumetric feature \mathcal{V} .

We design a self-3D attention given volumetric feature \mathcal{V} to encode the amount of blur in texture features and aggregate the matching cost in homogeneous regions [9]. The layer consists of several 3D convolutional layers and the Sigmoid function. This obtains a soft mask as an attention map \mathcal{W} and adaptively selects features along the channel where \mathcal{V} is concatenated. The soft mask \mathcal{W} is multiplied with the feature \mathcal{V} to sample useful features and the final feature volume \mathcal{V}_S is produced through a softmax layer. Finally, the sampled features with the sub-pixel shift, G^L and G^R , are obtained by averaging the volume \mathcal{V}_S .

4.3. Adaptive Normal Module

Facial surface normals are widely used for many applications such as relighting [44, 61]. For greater applicability of our pipeline, we design a CNN to infer both depth and surface normal information from DP images, which is the first attempt to the best of our knowledge. As shown in Fig. 7, the proposed surface normal estimator, Adaptive Normal Module (ANM), produces a surface normal map complementary to an estimated defocus-disparity map. We find that the joint learning for surface normal and defocus-disparity improves the overall performance.

The ANM consists of *surface sampling module* to capture surface by sampling the aggregated cost volume C_A and *deformable 3D convolutional layer* to consider dynamic ranges of neighbors to compute normal vectors.

According to [29], an accurately aggregated cost volume contains an implicit function representation of underlying surfaces for depth estimation. Since the surface normal mainly depends on the shape of the local surface, it is redundant to use all voxel embeddings in C_A for facial normal estimation. We thus sample the local surface from the aggregated volume C_A using the estimated disparity map (Eq. 2). Since the local surface is defined with the metric scale depth, we convert disparity to a depth map using Eq. 1 in Sec. 3.1 and provide this volumetric information with our network denoted as coordinate volume in Fig. 7.

Since a human face has a variety of curved local surfaces, we need to consider dynamic ranges of neighbors to extract a surface normal from the surface-aware sampled volume C_S in the previous stage. To do this, we introduce ANM module, inspired by a local plane assumption in [32, 33, 37]. Following the assumption, a small set of neighbor points forms a local plane. The surface normal can be obtained from this local plane. Since the local patch has arbitrary shapes and sizes composed with its sampled neighboring points, we use 3D deformable convolutions [55] to consider the neighboring points within the dynamic ranges. The

learnable offsets of the deformable convolution in 3D space allow us to adaptively sample neighbors and to find the best local plane. The final feature volume C_N is predicted after passing two 3D deformable convolution layers to extract surface normal information from the sampled volume C_S .

4.4. Depth and Normal Estimation

The aggregated volume C_A passes through a classifier to produce a final matching cost \mathcal{A} , and the softmax function $\sigma(\cdot)$ is applied to regress the defocus-disparity \hat{d} . Accordingly, we compute the disparity as follows:

$$\hat{d}_{u,v} = \sum_{m=1}^M d^m \cdot \sigma(\mathcal{A}_{u,v}^m), \quad (2)$$

where $\hat{d}_{u,v}$ is the defocus-disparity and $\mathcal{A}_{u,v}$ is the final matching cost at a pixel (u, v) . M and d^m are the range of defocus-disparity, and predefined discrete disparity labels, respectively, whose details are described in Sec. 4.5. Following [8], we minimize a disparity loss $\mathcal{L}_{\text{disp}}$ using a smooth L_1 loss as follows:

$$\mathcal{L}_{\text{disp}} = \frac{1}{H \cdot W} \sum_{u=1}^W \sum_{v=1}^H \text{smooth}_{L_1}(d_{u,v} - \hat{d}_{u,v}), \quad (3)$$

where $d_{u,v}$ is a ground-truth defocus-disparity at a pixel (u, v) converted from the ground-truth metric scale depth in Sec. 3.1.

For the surface normal estimation, shared 2D convolutions are applied to the feature volume C_N to regress a surface normal. The final convolutional layers follow the same structure of the baseline architecture in [29]. Finally, we train ANM by minimizing a cosine similarity normal loss $\mathcal{L}_{\text{normal}}$ as:

$$\mathcal{L}_{\text{normal}} = \frac{1}{H \cdot W} \sum_{u=1}^W \sum_{v=1}^H (1 - \mathbf{N}_{u,v} \cdot \hat{\mathbf{N}}_{u,v}), \quad (4)$$

where $\mathbf{N}_{u,v}$ and $\hat{\mathbf{N}}_{u,v}$ are a ground-truth, and a predicted facial normal at a pixel (u, v) .

Our StereoDPNet is fully supervised by our ground-truth depth/normal maps. The network is trained by minimizing the combination of the disparity and normal losses.

4.5. Implementation Details

The depth in our facial dataset ranges from 80 cm to 110 cm as described in Sec. 3.2 and the focus distance is about 97 cm. Therefore, our valid disparity range on original images is from -12 to 32 pixels. We note that the resolution of input images used is 1680×1120 , which is down-sampled four-fold due to GPU memory limitations. We thus set the minimum and maximum disparity of Eq. 2 to -4 and 12 pixels. We also set the number of levels in the cost volume M to 8, which represents a 0.5 pixel accuracy at least. We train our network with a batch size of four, and use Adam optimizer [28] starting from initial learning rate 10^{-4} with a constant decay of 0.5 at every 35 epochs.

Method	Absolute error metric [mm] ↓					Affine error metric [px] ↓			Accuracy metric ↑		
	AbsRel	AbsDiff	SqRel	RMSE	RMSElog	WMAE	WRMSE	1 - ρ	$\delta < 1.01$	$\delta < 1.01^2$	$\delta < 1.01^3$
PSMNet [8]	0.006	5.314	0.054	6.770	0.008	0.093	0.126	0.054	0.818	0.983	0.999
StereoNet [26]	0.005	4.306	0.038	5.811	0.006	0.112	0.150	0.087	0.903	0.991	0.999
DPNet [15]	0.008	7.175	0.092	8.833	0.010	0.110	0.148	0.086	0.688	0.959	0.911
MDD [36]	-	-	-	-	-	1.830	2.348	0.575	-	-	-
BTS [30]	0.007	6.575	0.081	8.102	0.009	0.111	0.150	0.077	0.731	0.964	0.995
NNet [29]	0.004	3.608	0.027	4.858	0.005	0.073	0.102	0.048	0.934	0.995	0.999
StereoDPNet (Ours)	0.003	2.864	0.019	3.899	0.004	0.064	0.091	0.034	0.966	0.995	0.999

Table 1. **Depth Benchmark Results.** We show that our proposed method outperforms the existing stereo matching methods (PSMNet [8], StereoNet [26]), DP-oriented state-of-the-art methods (DPNet [15], MDD [36]), monocular depth estimation (BTS [30]), and depth/normal network for stereo matching (NNet [29]). Note that since MDD adopts another a defocus-disparity geometry different from [15], it is not measured by the absolute metrics.

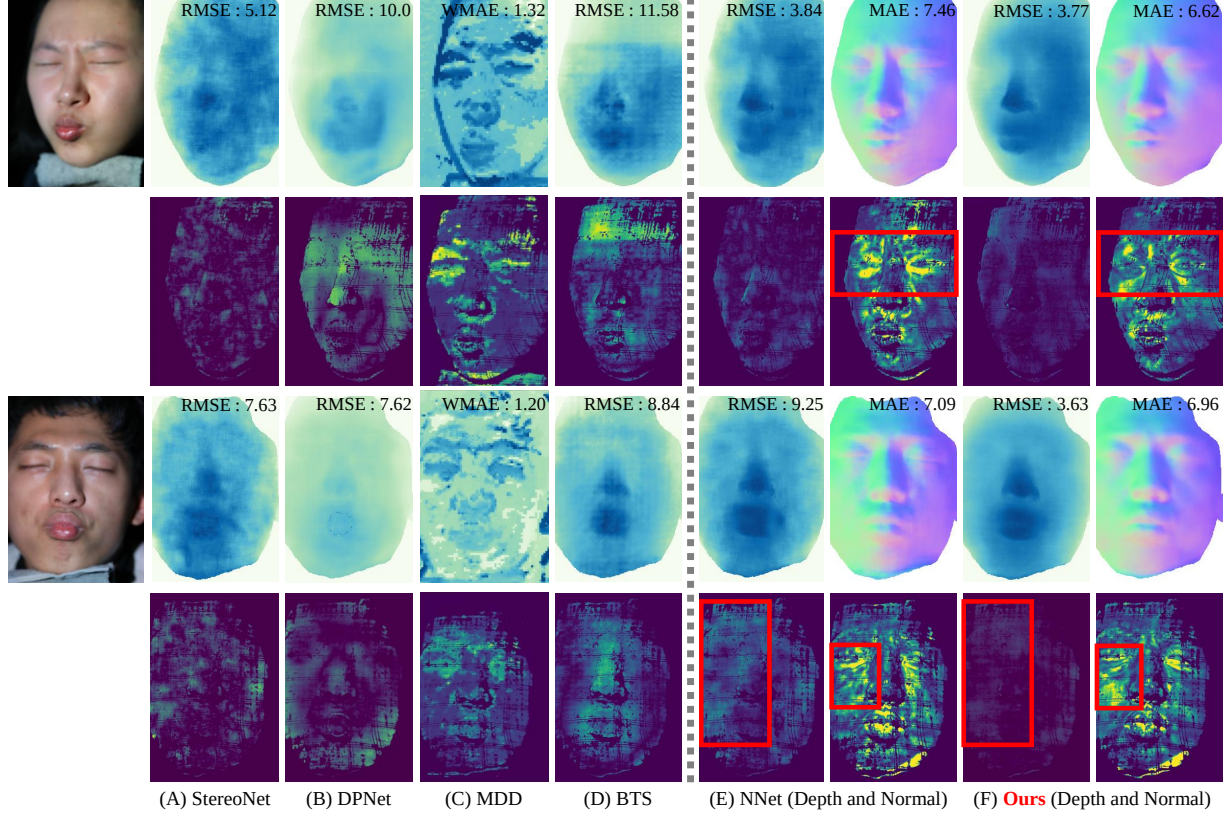


Figure 8. **Qualitative results on test set.** We report AbsRel map of depths and MAE map of normals as the error map of predictions. The error map from MDD is the WMAE map because it predicts relative scale depth maps. We note that the range of error map is 0.0 ~ 1.0 (AbsRel [mm]) and 0.0 ~ 15.0 (MAE [deg]).

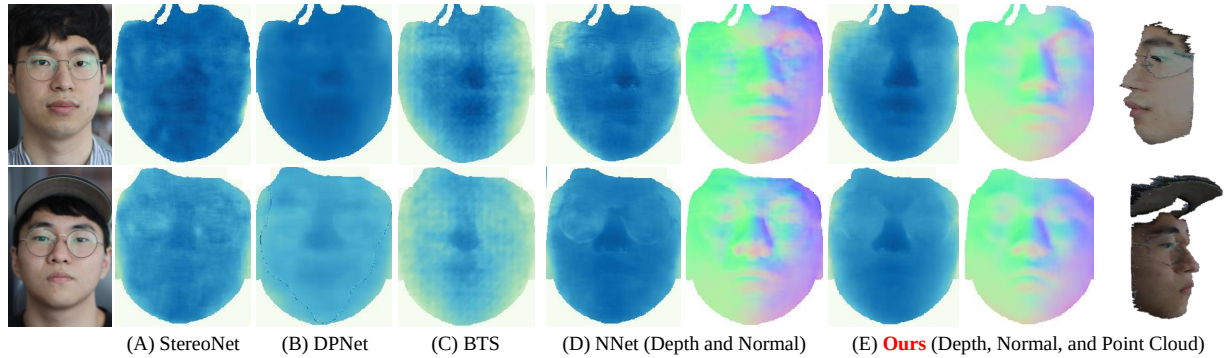


Figure 9. **Real-world results.** We capture several people in unmet real-world and compare our method with the others in Table 1. Our StereoDPNet clearly captures surface and boundary depth of the face. Please refer to the supplementary material to enjoy more examples.

Methods	ANM Modules		Absolute metric [mm] ↓		Affine metric [px] ↓			Accuracy metric ↑		Normal metric [deg] ↓	
	Sampling	Deform3D	AbsDiff	RMSE	WMAE	WRMSE	1 - ρ	$\delta < 1.01$	$\delta < 1.01^2$	MAE	RMSE
ASM Only			4.895	6.223	0.095	0.127	0.056	0.850	0.992	-	-
NNet [29]			3.608	4.858	0.073	0.102	0.048	0.934	0.995	9.634	11.877
ASM + NNet			3.271	4.434	0.064	0.090	0.033	0.947	0.997	9.072	11.045
ASM + NNet	✓		3.214	4.519	0.062	0.089	0.037	0.943	0.990	8.894	10.837
StereoDPNet	✓	✓	2.864	3.899	0.064	0.091	0.034	0.966	0.995	7.479	9.386

Table 2. **Ablation Study of ANM.** We note that NNet [29] is a baseline model of our overall architecture. We compare the performance of depth and surface normal estimation by adding each component.

Method	Absolute error metric [mm] ↓			Accuracy metric ↑	
	AbsDiff	SqRel	RMSE	$\delta < 1.01$	$\delta < 1.01^2$
Bilinear (Bi)	7.956	0.116	9.842	0.615	0.928
Phase	8.287	0.132	10.487	0.606	0.916
Phase + Bi	6.030	0.067	7.522	0.754	0.980
Nearest + Bi	5.841	0.062	7.287	0.772	0.984
Nearest + Phase	5.831	0.062	7.247	0.773	0.985
ASM	4.895	0.045	6.223	0.850	0.992

Table 3. **Ablation Study of ASM.** We test various sampling strategies in ASM and determine the final structure of ASM. Here, we only use ASM to strictly compare the inference of each sampling strategies. Bi denotes bilinear sampling.

5. Experiments

To evaluate the effectiveness and the robustness of our work, we carry out various experiments on our dataset as well as DP images captured under real-world environments. For a fair comparison, all the methods are trained on identical training sets of our dataset from scratch. We then evaluate the quality of estimated depth/normal maps on the same test split of our facial dataset. Note that we use the facial mask for training and the test, given by the data acquisition process in Sec. 3.2. For the real-world samples, we use a facial mask from a pretrained face segmentation network¹.

5.1. Evaluation Metrics

In our dataset benchmark, we convert our predicted disparity to depth (Sec. 3.1). Thus, we use both evaluation metrics in a public benchmark suite²: AbsRel, AbsDiff, SqRel, RMSE, RMSElog, and inlier pixel ratios ($\delta < 1.01^i$ where $i \in \{1, 2, 3\}$)³ and affine invariant metrics [15] for the evaluation of predicted disparity/depth. To measure the quality of a surface normal map, we utilize a Mean Angular Error (MAE) and a Root Mean Square Angular Error (RMSAE) in degree unit following the DiLiGenT benchmark [45].

5.2. Comparison Results

Depth Benchmark. We compare our method with recent DP-based depth estimation approaches, DPNet [15] and MDD [36], as well as widely used stereo matching networks including PSMNet [8] and StereoNet [26], a depth/normal

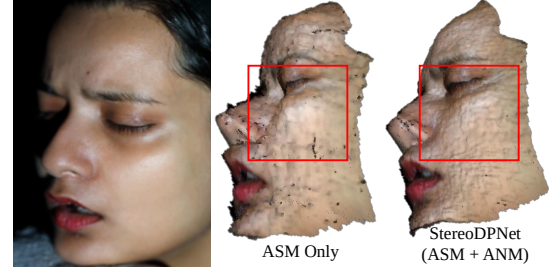


Figure 10. **Surface refinement with Adaptive Normal Module.** We compare 3D point cloud of the method of only adding ASM with our full method of ASM and ANM. Our ANM refines surface via cost volume and this leads to major performance improvement.

network for stereo matching, NNet [29] and a state-of-the-art monocular depth estimation network, BTS [30], whose results are reported in Table 1 and in Fig. 8. Since there is no published code for [15], we implement DPNet [15] to predict disparity instead of inverse depth following them, and check that the performance is similar on their dataset.

Due to the small range of the defocus-disparity from DP images (-4px to 12px), the cost volume with the discrete hypotheses leads to unstable training [60]. As a result, typical depth estimations, PSMNet and BTS, and the DP-oriented methods, DPNet and MDD, do not work well. For example, both DPNet and BTS suffer from blurry predictions, and MDD [36] is sensitive to the textureless regions in human faces. Although both NNet [29] and StereoNet [26] show relatively promising results, our method still outperforms them. Nevertheless, the edge-awareness of StereoNet is worth considering for refinement of our framework.

In addition, we compare various subpixel sampling strategies in ASM as an ablation study. In Table 3, including whole attention maps from three different interpolations as proposed in ASM, shows the best performance over any combination of two interpolations. Moreover, our surface normal estimation greatly improves the prediction of the disparity in Table 2. We attribute this outstanding performance to our two sub-modules (ASM and ANM), which overcome the extremely narrow baselines in DP images.

Surface Normal Benchmark. To the best of our knowledge, this is the first attempt to estimate both the surface normal and the defocus-disparity from single DP images. Since the basic structure of ANM is derived from the recent depth and normal network [29] for multi-view stereo, we show the performance improvement of our ANM, com-

¹<https://github.com/zllrunning/face-parsing.pytorch>

²<http://www.cvlibs.net/datasets/kitti/>

³All equations of the metrics are described in Supplementary material.

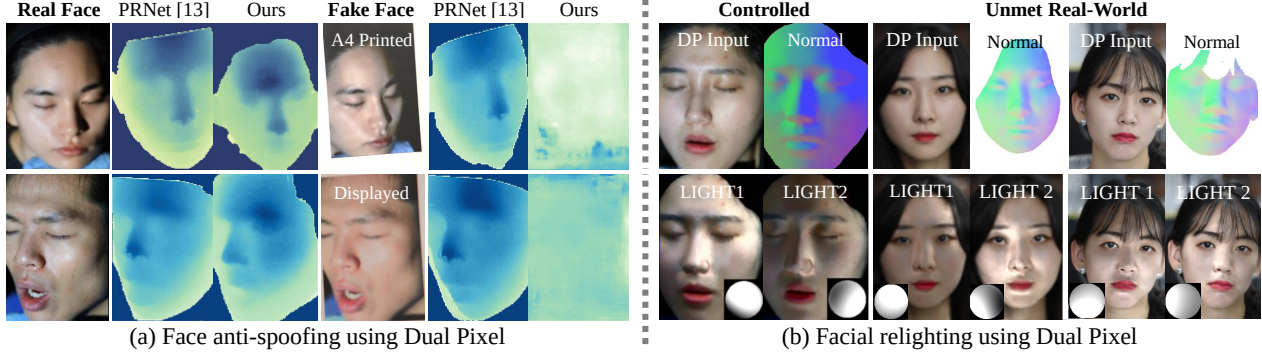


Figure 11. **Applications.** (a) To show the application to face anti-spoofing, StereoDPNet infers depth maps with the real and fake face samples (paper attack and display attack). Note that the depth maps from StereoDPNet allow the face detector to distinguish whether the input is a real face or not because it computes correspondences between two DP images. (b) We display the original DP image, estimated normal map from StereoDPNet, and two different relit images with sampled lighting directions.

Method	Acc \uparrow	ACER \downarrow	FP	FN
PRNet [13]	62.815	0.5083	38	97
Ours	100.0	0.0000	0	0

Table 4. **Face spoof detection results** Evaluation results from a pretrained FeatherNet using depth from PRNet (Monocular) and Ours (DP data) on 608 true and 266 fake samples. ACER is the error rate of classifying face widely used in [49, 57]. FP and FN denote False Positive and False Negative sample numbers.

pared to the baseline method [29] by adding each component in Table 2. We find that joint learning of disparity and surface normal leads to geometrically consistent and high-quality depth and surface normal shown in Fig. 10, which has been demonstrated in previous works [22, 38].

Real World Experiment. To verify the generalizability of our method, we newly capture outdoor DP images using the Canon DSLR camera, as shown in Fig. 9. Surprisingly, our StereoDPNet trained on our facial dataset also works well with general scenes (Fig. 12), which demonstrates that our network is generalized well.

5.3. Applications

Face Spoofing Detection. We first show an application to face spoofing detection. Unlike the previous work [49] using a single image depth, our method facilitates parallax cue for depth estimation from DP sensors. To validate that our dataset and model are applicable to this task, we use a pretrained detector [57] trained on the CASIA-SURF dataset [58], which depends solely on input facial depth data to determine whether the depth is from a real face image. The quantitative evaluation in Table 4 and qualitative results in Fig. 11 (a) show that the detector [57] mostly fails to recognize the fake faces given the single image depth estimated by PRNet [49]. Meanwhile, the real and fake images are successfully classified when the detector takes the depth maps from our network. We also refer to a recent study [52] for face anti-spoofing using DP. We expect that our dataset will be useful for this research field.

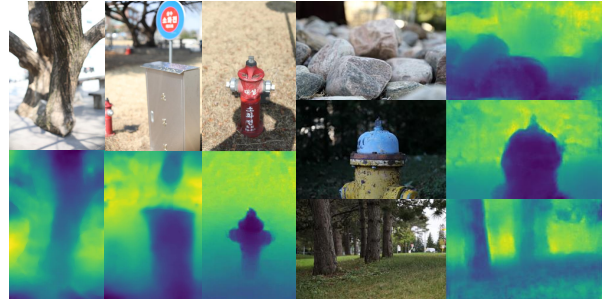


Figure 12. **Depth from single DP images in the wild.** We show depth estimation results of StereoDPNet on outdoor photos, which are directly captured by us (left side) and in a public real-world DP dataset [2] for deblurring (right side).

Face Relighting. Given the reference images and the surface normals from StereoDPNet, we generate relighted images using a Ratio Image-based method [61]. The target spherical harmonic lightings are randomly sampled and the lighting directions of reference images are inferred with SfSNet [42], whose results are displayed in Fig. 11 (b).

6. Conclusion

We present a high-quality facial DP dataset incorporating 135,744 face images for 101 subjects with corresponding depth maps in metric scale and surface normal maps. Moreover, we introduce DP-oriented StereoDPNet for both depth and surface normal estimation. The proposed StereoDPNet successfully shows impressive results in the wild by effectively handling the narrow baseline problem in DP.

Potential societal impact. We have already received consents from participants to use our facial dataset for only academic purposes. Thus, our dataset will be available to the computer vision community to promote relevant research.

Limitation. Our dataset is captured in a fixed range of defocus-disparity of about -12 to 32 pixels. Although one can adjust the focus distance and calibrate camera parameters to cover various scene depths, we cannot cover scenes with wide disparity ranges. We note that our network sometimes fails to capture transparent objects such as glasses.

References

- [1] Henrik Aanæs, Rasmus Ramsbøl Jensen, George Vogiatzis, Engin Tola, and Anders Bjarholm Dahl. Large-scale data for multiple-view stereopsis. *Proceedings of the IEEE/CVF International Conference on Computer Vision (ICCV)*, pages 1–16, 2016. [3](#)
- [2] Abdullah Abuolaim and Michael S Brown. Defocus deblurring using dual-pixel data. In *Proceedings of the European conference on computer vision (ECCV)*, pages 111–126. Springer, 2020. [3](#), [8](#)
- [3] Abdullah Abuolaim, Mauricio Delbracio, Damien Kelly, Michael S Brown, and Peyman Milanfar. Learning to reduce defocus blur by realistically modeling dual-pixel data. In *Proceedings of the IEEE/CVF International Conference on Computer Vision (ICCV)*, pages 2289–2298, 2021. [2](#), [3](#)
- [4] Apple. Apple iphone 11 pro. <https://www.apple.com/iphone-11-pro/>, 2019. Accessed: 2019-09-20. [1](#)
- [5] ARCore. Augmented faces. <https://developers.google.com/ar/develop/java/augmented-faces>, 2019. Accessed: 2019-12-18. [1](#)
- [6] Ziqian Bai, Zhaopeng Cui, Jamal Ahmed Rahim, Xiaoming Liu, and Ping Tan. Deep facial non-rigid multi-view stereo. In *Proceedings of the IEEE/CVF Conference on Computer Vision and Pattern Recognition (CVPR)*, pages 5850–5860, 2020. [2](#)
- [7] Volker Blanz and Thomas Vetter. A morphable model for the synthesis of 3d faces. In *Proceedings of the 26th annual conference on Computer graphics and interactive techniques*, pages 187–194, 1999. [2](#)
- [8] Jia-Ren Chang and Yong-Sheng Chen. Pyramid stereo matching network. In *Proceedings of the IEEE/CVF Conference on Computer Vision and Pattern Recognition (CVPR)*, 2018. [4](#), [5](#), [6](#), [7](#)
- [9] Ching-Hui Chen, Hui Zhou, and Timo Ahonen. Blur-aware disparity estimation from defocus stereo images. In *Proceedings of the IEEE/CVF International Conference on Computer Vision (ICCV)*, pages 855–863, 2015. [4](#), [5](#)
- [10] Liang-Chieh Chen, Yukun Zhu, George Papandreou, Florian Schroff, and Hartwig Adam. Encoder-decoder with atrous separable convolution for semantic image segmentation. In *Proceedings of the European conference on computer vision (ECCV)*, 2018. [4](#)
- [11] Wenzheng Chen, Parsa Mirdehghan, Sanja Fidler, and Kiriakos N Kutulakos. Auto-tuning structured light by optical stochastic gradient descent. In *Proceedings of the IEEE/CVF Conference on Computer Vision and Pattern Recognition (CVPR)*, 2020. [3](#)
- [12] Yu Deng, Jialong Yang, Sicheng Xu, Dong Chen, Yunde Jia, and Xin Tong. Accurate 3d face reconstruction with weakly-supervised learning: From single image to image set. In *Proceedings of the IEEE/CVF Conference on Computer Vision and Pattern Recognition (CVPR) Workshops*, June 2019. [2](#)
- [13] Yao Feng, Fan Wu, Xiaohu Shao, Yanfeng Wang, and Xi Zhou. Joint 3d face reconstruction and dense alignment with position map regression network. In *Proceedings of the European conference on computer vision (ECCV)*, 2018. [2](#), [8](#)
- [14] Galaxy. Samsung galaxy s10. <https://www.samsung.com/us/mobile/galaxy-s10/>, 2019. Accessed: 2019-03-08. [1](#)
- [15] Rahul Garg, Neal Wadhwa, Sameer Ansari, and Jonathan T Barron. Learning single camera depth estimation using dual-pixels. In *Proceedings of the IEEE/CVF International Conference on Computer Vision (ICCV)*, 2019. [2](#), [3](#), [6](#), [7](#)
- [16] Google. Google photos: One year, 200 million users, and a whole lot of selfies. <https://blog.google/products/photos/google-photos-one-year-200-million/>, 2016. Accessed: 2016-05-27. [1](#)
- [17] Google. More controls and transparency for your selfies. <https://blog.google/outreach-initiatives/digital-wellbeing/more-controls-selfie-filters/>, 2020. Accessed: 2020-10-01. [1](#)
- [18] Jianzhu Guo, Xiangyu Zhu, Yang Yang, Fan Yang, Zhen Lei, and Stan Z Li. Towards fast, accurate and stable 3d dense face alignment. In *Proceedings of the European conference on computer vision (ECCV)*, pages 152–168. Springer, 2020. [2](#)
- [19] Hyowon Ha, Tae-Hyun Oh, and In So Kweon. A multi-view structured-light system for highly accurate 3d modeling. In *International Conference on 3D Vision (3DV)*, 2015. [3](#)
- [20] Hyowon Ha, Jaesik Park, and In So Kweon. Dense depth and albedo from a single-shot structured light. In *International Conference on 3D Vision (3DV)*, pages 127–134, 2015. [3](#)
- [21] Yudeog Han, Joon-Young Lee, and In So Kweon. High quality shape from a single rgb-d image under uncalibrated natural illumination. In *Proceedings of the IEEE/CVF International Conference on Computer Vision (ICCV)*, 2013. [3](#)
- [22] Sunghoon Im, Hyowon Ha, Gyeongmin Choe, Hae-Gon Jeon, Kyungdon Joo, and In So Kweon. High quality structure from small motion for rolling shutter cameras. In *Proceedings of the IEEE/CVF International Conference on Computer Vision (ICCV)*, 2015. [8](#)
- [23] Rasmus Jensen, Anders Dahl, George Vogiatzis, Engin Tola, and Henrik Aanæs. Large scale multi-view stereopsis evaluation. In *Proceedings of the IEEE/CVF Conference on Computer Vision and Pattern Recognition (CVPR)*, 2014. [3](#)
- [24] Hae-Gon Jeon, Jaesik Park, Gyeongmin Choe, Jinsun Park, Yunsu Bok, Yu-Wing Tai, and In So Kweon. Accurate depth map estimation from a lenslet light field camera. In *Proceedings of the IEEE/CVF Conference on Computer Vision and Pattern Recognition (CVPR)*, 2015. [4](#), [5](#)
- [25] Leonid Keselman, John Iselin Woodfill, Anders Grunnet-Jepsen, and Achintya Bhowmik. Intel realsense stereoscopic depth cameras. In *Proceedings of the IEEE/CVF Conference on Computer Vision and Pattern Recognition (CVPR) Workshops*, 2017. [1](#)
- [26] Sameh Khamis, Sean Fanello, Christoph Rhemann, Adarsh Kowdle, Julien Valentin, and Shahram Izadi. Stereonet: Guided hierarchical refinement for real-time edge-aware depth prediction. In *Proceedings of the European Conference on Computer Vision (ECCV)*, pages 573–590, 2018. [4](#), [6](#), [7](#)

- [27] Kinect2. Kinect for windows sdk 2.0. <https://developer.microsoft.com/en-us/windows/kinect/>, 2014. Accessed: 2014-10-21. 1
- [28] Diederik P Kingma and Jimmy Ba. Adam: A method for stochastic optimization. *arXiv preprint arXiv:1412.6980*, 2014. 5
- [29] Uday Kusupati, Shuo Cheng, Rui Chen, and Hao Su. Normal assisted stereo depth estimation. In *Proceedings of the IEEE/CVF Conference on Computer Vision and Pattern Recognition (CVPR)*, 2020. 5, 6, 7, 8
- [30] Jin Han Lee, Myung-Kyu Han, Dong Wook Ko, and Il Hong Suh. From big to small: Multi-scale local planar guidance for monocular depth estimation. *arXiv preprint arXiv:1907.10326*, 2019. 6, 7
- [31] Tsung-Yi Lin, Piotr Dollár, Ross Girshick, Kaiming He, Bharath Hariharan, and Serge Belongie. Feature pyramid networks for object detection. In *Proceedings of the IEEE/CVF Conference on Computer Vision and Pattern Recognition (CVPR)*, 2017. 4
- [32] Xiaoxiao Long, Cheng Lin, Lingjie Liu, Wei Li, Christian Theobalt, Ruigang Yang, and Wenping Wang. Adaptive surface normal constraint for depth estimation. *Proceedings of the IEEE/CVF International Conference on Computer Vision (ICCV)*, 2021. 5
- [33] Xiaoxiao Long, Lingjie Liu, Christian Theobalt, and Wenping Wang. Occlusion-aware depth estimation with adaptive normal constraints. In *Proceedings of the European conference on computer vision (ECCV)*, pages 640–657. Springer, 2020. 5
- [34] Diego Nehab, Szymon Rusinkiewicz, James Davis, and Ravi Ramamoorthi. Efficiently combining positions and normals for precise 3d geometry. *ACM Transactions on Graphics (ToG)*, 24(3):536–543, 2005. 3
- [35] Liyuan Pan, Shah Chowdhury, Richard Hartley, Miaomiao Liu, Hongguang Zhang, and Hongdong Li. Dual pixel exploration: Simultaneous depth estimation and image restoration. In *Proceedings of the IEEE/CVF Conference on Computer Vision and Pattern Recognition (CVPR)*, pages 4340–4349, June 2021. 2, 3
- [36] Abhijith Punnappurath, Abdullah Abuolaim, Mahmoud Afifi, and Michael S Brown. Modeling defocus-disparity in dual-pixel sensors. In *2020 IEEE International Conference on Computational Photography (ICCP)*, 2020. 2, 6, 7
- [37] Xiaojuan Qi, Renjie Liao, Zhengzhe Liu, Raquel Urtasun, and Jiaya Jia. Geonet: Geometric neural network for joint depth and surface normal estimation. In *Proceedings of the IEEE/CVF Conference on Computer Vision and Pattern Recognition (CVPR)*, pages 283–291, 2018. 5
- [38] Jiaxiong Qiu, Zhaopeng Cui, Yinda Zhang, Xingdi Zhang, Shuaicheng Liu, Bing Zeng, and Marc Pollefeys. DeepLidar: Deep surface normal guided depth prediction for outdoor scene from sparse lidar data and single color image. In *Proceedings of the IEEE/CVF Conference on Computer Vision and Pattern Recognition (CVPR)*, 2019. 8
- [39] Elad Richardson, Matan Sela, Roy Or-El, and Ron Kimmel. Learning detailed face reconstruction from a single image. In *Proceedings of the IEEE/CVF Conference on Computer Vision and Pattern Recognition (CVPR)*, pages 1259–1268, 2017. 2
- [40] Daniel Scharstein and Richard Szeliski. High-accuracy stereo depth maps using structured light. In *Proceedings of the IEEE/CVF Conference on Computer Vision and Pattern Recognition (CVPR)*, volume 1, 2003. 3
- [41] Johannes L Schönberger, Enliang Zheng, Jan-Michael Frahm, and Marc Pollefeys. Pixelwise view selection for unstructured multi-view stereo. In *Proceedings of the European conference on computer vision (ECCV)*, 2016. 2
- [42] Soumyadip Sengupta, Angjoo Kanazawa, Carlos D Castillo, and David W Jacobs. Sfsnet: Learning shape, reflectance and illuminance of faces in the wild. In *Proceedings of the IEEE/CVF Conference on Computer Vision and Pattern Recognition (CVPR)*, 2018. 8
- [43] Jiaxiang Shang, Tianwei Shen, Shiwei Li, Lei Zhou, Mingmin Zhen, Tian Fang, and Long Quan. Self-supervised monocular 3d face reconstruction by occlusion-aware multi-view geometry consistency. In *Proceedings of the European conference on computer vision (ECCV)*, pages 53–70. Springer, 2020. 2
- [44] Amnon Shashua and Tammy Riklin-Raviv. The quotient image: Class-based re-rendering and recognition with varying illuminations. *IEEE Transactions on Pattern Analysis and Machine Intelligence*, 23(2):129–139, 2001. 5
- [45] Boxin Shi, Zhe Wu, Zhipeng Mo, Dinglong Duan, Sai-Kit Yeung, and Ping Tan. A benchmark dataset and evaluation for non-lambertian and uncalibrated photometric stereo. In *Proceedings of the IEEE/CVF Conference on Computer Vision and Pattern Recognition (CVPR)*, 2016. 7
- [46] N. Silberman and R. Fergus. Indoor scene segmentation using a structured light sensor. In *Proceedings of the IEEE/CVF International Conference on Computer Vision (ICCV) - Workshop on 3D Representation and Recognition*, 2011. 3
- [47] Luan Tran and Xiaoming Liu. Nonlinear 3d face morphable model. In *Proceedings of the IEEE/CVF Conference on Computer Vision and Pattern Recognition (CVPR)*, pages 7346–7355, 2018. 2
- [48] Neal Wadhwa, Rahul Garg, David E Jacobs, Bryan E Feldman, Nori Kanazawa, Robert Carroll, Yair Movshovitz-Attias, Jonathan T Barron, Yael Pritch, and Marc Levoy. Synthetic depth-of-field with a single-camera mobile phone. *ACM Transactions on Graphics (ToG)*, 37(4):1–13, 2018. 2
- [49] Zezheng Wang, Zitong Yu, Chenxu Zhao, Xiangyu Zhu, Yunxiao Qin, Qiusheng Zhou, Feng Zhou, and Zhen Lei. Deep spatial gradient and temporal depth learning for face anti-spoofing. In *Proceedings of the IEEE/CVF Conference on Computer Vision and Pattern Recognition (CVPR)*, 2020. 8
- [50] Fanzi Wu, Linchao Bao, Yajing Chen, Yonggen Ling, Yibing Song, Songnan Li, King Ng Ngan, and Wei Liu. Mvf-net: Multi-view 3d face morphable model regression. In *Proceedings of the IEEE/CVF Conference on Computer Vision and Pattern Recognition (CVPR)*, pages 959–968, 2019. 2
- [51] Shangzhe Wu, Christian Rupprecht, and Andrea Vedaldi. Unsupervised learning of probably symmetric deformable

- 3d objects from images in the wild. In *Proceedings of the IEEE/CVF Conference on Computer Vision and Pattern Recognition (CVPR)*, 2020. 2
- [52] Xiaojun Wu, Jinghui Zhou, Jun Liu, Fangyi Ni, and Haoqiang Fan. Single-shot face anti-spoofing for dual pixel camera. *IEEE Transactions on Information Forensics and Security*, 16:1440–1451, 2020. 2, 8
- [53] Haofei Xu and Juyong Zhang. Aanet: Adaptive aggregation network for efficient stereo matching. In *Proceedings of the IEEE/CVF Conference on Computer Vision and Pattern Recognition (CVPR)*, pages 1959–1968, 2020. 4
- [54] Fei Yang, Jue Wang, Eli Shechtman, Lubomir Bourdev, and Dimitri Metaxas. Expression flow for 3d-aware face component transfer. In *ACM SIGGRAPH 2011 papers*, pages 1–10. 2011. 1
- [55] Xinyi Ying, Longguang Wang, Yingqian Wang, Weidong Sheng, Wei An, and Yulan Guo. Deformable 3d convolution for video super-resolution. *IEEE Signal Processing Letters*, 27:1500–1504, 2020. 5
- [56] Feihu Zhang, Victor Prisacariu, Ruigang Yang, and Philip HS Torr. Ga-net: Guided aggregation net for end-to-end stereo matching. In *Proceedings of the IEEE/CVF Conference on Computer Vision and Pattern Recognition (CVPR)*, pages 185–194, 2019. 4
- [57] Peng Zhang, Fuhao Zou, Zhiwen Wu, Nengli Dai, Skarpmess Mark, Michael Fu, Juan Zhao, and Kai Li. Feather-nets: Convolutional neural networks as light as feather for face anti-spoofing. In *Proceedings of the IEEE/CVF Conference on Computer Vision and Pattern Recognition (CVPR) Workshops*, 2019. 8
- [58] Shifeng Zhang, Ajian Liu, Jun Wan, Yanyan Liang, Guodong Guo, Sergio Escalera, Hugo Jair Escalante, and Stan Z Li. Casia-surf: A large-scale multi-modal benchmark for face anti-spoofing. *IEEE Transactions on Biometrics, Behavior, and Identity Science*, 2(2):182–193, 2020. 8
- [59] Shifeng Zhang, Xiaobo Wang, Ajian Liu, Chenxu Zhao, Jun Wan, Sergio Escalera, Hailin Shi, Zezheng Wang, and Stan Z Li. A dataset and benchmark for large-scale multi-modal face anti-spoofing. In *Proceedings of the IEEE/CVF Conference on Computer Vision and Pattern Recognition (CVPR)*, 2019. 1
- [60] Yinda Zhang, Neal Wadhwa, Sergio Orts-Escolano, Christian Häne, Sean Fanello, and Rahul Garg. Du 2 net: Learning depth estimation from dual-cameras and dual-pixels. In *Proceedings of the European conference on computer vision (ECCV)*, pages 582–598. Springer, 2020. 2, 7
- [61] Hao Zhou, Sunil Hadap, Kalyan Sunkavalli, and David W Jacobs. Deep single-image portrait relighting. In *Proceedings of the IEEE/CVF International Conference on Computer Vision (ICCV)*, 2019. 1, 2, 5, 8